Tropical cyclone evolution in a minimal axisymmetric model revisited

Christoph W. Schmidt[a] and Roger K. Smith[a]

[a] *Meteorological Institute, Ludwig-Maximilians University of Munich, Munich, Germany*

*Correspondence to: Roger K. Smith, Meteorological Institute, Ludwig-Maximilians University of Munich, Theresienstr. 37, 80333 Munich, Germany. Email: roger.smith@lmu.de

An improved version of a minimal model for a tropical cyclone is described. The model is used to revisit some fundamental aspects of vortex behaviour in the prototype problem for tropical cyclone intensification. After rapidly intensifying to a mature phase in which the maximum tangential wind speed remains quasi-steady for a few days, the vortex ultimately decays. In a 20 day simulation, the vortex never becomes globally-steady. In particular, the upper anticyclone continues to expand for the duration of the integration. These results are consistent with those of recent studies using more sophisticated numerical models. As in the latter models, an important feature of the dynamics of spin up is the development of supergradient winds in the boundary layer and the vertical advection of the associated high tangential-momentum air from the boundary layer to spin up the eyewall region. This mechanism, while consistent with some recently reported results, is not part of the classical theory of spin up. Copyright ⓒ 2015 Royal Meteorological Society

1. Introduction

Simple models occupy an important niche in providing basic understanding of tropical cyclone behaviour. Indeed, three of the early paradigms for tropical cyclone intensification are based on minimal models with a simplified representations of the physical processes thought to be of most importance (Charney and Eliassen 1964, Ooyama 1969, Emanuel 1989, 1997). A recent review of these paradigms is given by Montgomery and Smith (2014).

More than a decade ago, Zhu *et al.* (2001) described one such minimal numerical model, a three-dimensional, three-layer, model formulated in σ-coordinates. The model was designed initially to examine the sensitivity of tropical cyclone intensification to different convective parameterization schemes in the same model and in a configuration that was simple enough to provide insight into the differences between schemes in relation to the intensification process. A novel feature of the model was the ability to switch from one mass-flux cumulus parameterization scheme to another by simply changing the method for determining the cloud base mass flux.

An axisymmetric version of the Zhu *et al.* model was developed by Nguyen *et al.* (2002) and a slightly modified version thereof was used more recently by Smith *et al.* (2011) to explore the effects of latitude on tropical cyclone intensity and size. In the latter study, the model was run for a period of 12 days, by which time the vortex appeared to have reached a quasi-steady state as judged by the evolution of the maximum tangential wind speed. Based on the behaviour of previous simple models, a quasi-steady solution was to be expected and was not questioned. Very recently, however, the issue of *globally steady-state* tropical cyclone solutions has come under close scrutiny (Smith *et al.* 2014a) because of the need in such models to replenish the cyclonic angular momentum lost to the system by friction at the sea surface (Anthes 1972). Thus, one motivation of the present study is to establish whether the solutions obtained in previous versions of the minimal model were globally steady and, if so, to identify the source of angular momentum.

In more sophisticated three-dimensional, multi-layer models discussed by Smith *et al.* (2014a) and Kilroy *et*

al. (2015), a global steady state was not achieved and after going through a mature phase in which the maximum tangential wind speed remained quasi-steady for a few days, the vortex ultimately decayed. Moreover, the upper anticyclone continued to evolve, even during the mature stage so that the vortex was not globally quasi-steady. Here we investigate this issue with a modified version of the minimal axisymmetric model of Smith *et al.* (2011).

A further issue with previous versions of the minimal model, again only recently discovered, is that the surface enthalpy fluxes are unrealistically large, a feature that is attributable to the assumption of a well-mixed boundary layer (the lowest layer of the minimal model). The problem arises because, in a conventional bulk formulation, the surface moisture flux is assumed to be proportional to the difference between the saturation specific humidity at the sea surface temperature and the specific humidity at a height of 10 m above the surface. Assuming that the specific humidity in the boundary layer is well mixed, as is done also in the Emanuel formulations (Emanuel 1989, 1997, 2003, 2012), the specific humidity at a height of 10 m can be equated with that throughout the boundary layer. However, the results from models with a more sophisticated representation of the boundary layer suggest that this may be a poor approximation, except possibly for a small range of radii inside the radius of maximum tangential wind speed (see e.g. Rotunno and Emanuel 1987, their Figure 12 and Montgomery *et al.* 2014, their Figure 14[*]). A further examination of this issue provides additional motivation for the present paper.

A final aim of the paper is to compare our results with those of a recent study by Kilroy *et al.* (2015), which uses a more sophisticated three-dimensional model. They showed that tropical cyclones grow progressively in size and decay in intensity after reaching maturity. We examine whether such behaviour is a feature of the minimal model.

The paper is organized as follows. The model and the details of the numerical simulation carried out are described in sections 2 and 3. The results of the simulation are presented and discussed in sections 5 and 6, respectively. The conclusions are given in section 7.

2. Description of the numerical model

2.1. Governing equations

The model used here is an axisymmetric version of the minimal three-layer hurricane model described by Zhu *et al.* (2001), similar to that developed by Nguyen *et al.* (2002). The formulation is based on the hydrostatic primitive equations in cylindrical σ-coordinates (r, λ, σ) on an f-plane, where $\sigma = (p - p_{top})/p^*$, $p^* = p_s - p_{top}$, p_s and p_{top} are the surface and top pressures, respectively, p_{top} is a constant (taken here to be 100 mb), and f is the Coriolis parameter. The lower interface σ-level is 8/9 and the upper one is 3/9. The upper and lower boundary conditions require that $\dot{\sigma} = 0$ at $\sigma = 0$ and $\sigma = 1$, where $\dot{\sigma} = D\sigma/Dt$ is the 'vertical' σ-velocity and D/Dt is the material derivative. The radial and tangential momentum equations and the hydrostatic equation are:

$$\frac{\partial u}{\partial t} = -u\frac{\partial u}{\partial r} - \dot{\sigma}\frac{\partial u}{\partial \sigma} + fv + \frac{v^2}{r} + \frac{R\theta\sigma(p^*\sigma + p_{top})^{\kappa-1}}{p_0^\kappa}\frac{\partial p^*}{\partial r} - \frac{\partial \phi}{\partial r} + D_u, \tag{1}$$

$$\frac{\partial v}{\partial t} = -u\frac{\partial v}{\partial r} - \dot{\sigma}\frac{\partial v}{\partial \sigma} - fu - \frac{uv}{r} + D_v, \tag{2}$$

$$\frac{\partial \phi}{\partial \sigma} = -\frac{Rp^*(p^*\sigma + p_{top})^\kappa}{p_0^\kappa}\theta, \tag{3}$$

where u and v are velocity components in the radial and tangential directions, R is the specific gas constant for dry air, $\kappa = R/c_p$, c_p is the specific heat of dry air, θ is the potential temperature, ϕ is the geopotential, and D_u and D_v represent terms associated with turbulence in the radial and azimuthal directions, respectively, and $p_0 = 1000$ mb.

The surface pressure tendency equation, derived from the continuity equation and boundary conditions is

$$\frac{\partial p^*}{\partial t} = -\int_0^1 \frac{1}{r}\frac{\partial}{\partial r}(p^*ru)d\sigma, \tag{4}$$

and $\dot{\sigma}$ is given by

$$\dot{\sigma} = -\frac{1}{p^*}\int_0^\sigma \frac{1}{r}\frac{\partial}{\partial r}(p^*ru)d\sigma + \frac{\sigma}{p^*}\int_0^1 \frac{1}{r}\frac{\partial}{\partial r}(p^*ru)d\sigma. \tag{5}$$

The thermodynamic and moisture equations are

$$\frac{\partial \theta}{\partial t} = -u\frac{\partial \theta}{\partial r} - \dot{\sigma}\frac{\partial \theta}{\partial \sigma} + Q_\theta + D_\theta + R_\theta \tag{6}$$

and

$$\frac{\partial q}{\partial t} = -u\frac{\partial q}{\partial r} - \dot{\sigma}\frac{\partial q}{\partial \sigma} + Q_q + D_q + R_q, \tag{7}$$

where θ is the potential temperature, q is the specific humidity, Q_θ and Q_q represent the diabatic heat and moisture sources associated with deep cumulus convection, and D_θ and D_q denote contributions from turbulence. The terms R_θ and R_q represent relaxation of the potential temperature and moisture to the prescribed environmental profiles. The temperature T is related to θ by

$$T = \left(\frac{p}{p_0}\right)^\kappa \theta = \frac{(p^*\sigma + p_{top})^\kappa}{p_0^\kappa}\theta. \tag{8}$$

2.2. Parameterization of turbulence

2.2.1. Surface turbulent fluxes

The turbulent flux of momentum to the sea surface and the surface fluxes of sensible and latent heat are represented by bulk aerodynamic formulae in the form

$$\begin{aligned}(F_u, F_v) &= -\rho C_D |\mathbf{u_b}| (u_b, v_b) \\ F_{sh} &= \rho c_p C_K |\mathbf{u_b}| (T_s - T_{air}) \\ F_q &= \rho C_K |\mathbf{u_b}| (q_s^* - q_{air}),\end{aligned} \tag{9}$$

where the subscript 'b' denotes the value at the middle of the boundary layer, $|\mathbf{u_b}|$ is the horizontal wind speed, T_s and q_s^* are the sea surface temperature (set to $28°C$) and the

---

[*]This figure shows an appreciable negative vertical gradient of equivalent potential temperature in the boundary layer which stems from a negative gradient of specific humidity there.

saturated specific humidity at this temperature (and at sea surface pressure), respectively. Furthermore, ρ denotes the near-surface air density, C_D is the surface drag coefficient, and C_K is the exchange coefficient for enthalpy.

In an earlier version of the minimal model, it was assumed that the specific humidity is well mixed and hence constant throughout the boundary layer as is done in the Emanuel formulations (Emanuel 1989, 1997, 2003, 2012). It was found recently that, at least in the present model, this assumption leads to surface moisture fluxes that are unrealistically large. To circumvent this problem, we use here a value for q_{air} that is linearly interpolated to a height of 250 m above sea surface, a value that was found to give reasonable flux values. As a guidance for realistic values, we followed an observational study by Cione *et al.* (2000) (see their Fig. 7).

In an earlier paper (Smith *et al.* 2011), the temperature near the surface, T_{air}, was obtained by extrapolating T_b along a dry adiabat to the 2-m level above the sea surface. This extrapolation was not done in older versions of the model, where T_b was used instead. Here we use a linearly interpolated value for T_{air} similar to that for q_{air} and in order to obtain realistic values of the Bowen ratio, we interpolate T_{air} to a height of 150 m, i.e., 100 m lower than the height of interpolated value of q_{air}.

As a precautionary means to inhibit the development of parameterized deep convection in the outer-core region over this extended period of integration, we set the surface sensible and latent heat fluxes to zero beyond a radius of 500 km. However, we did carry out a calculation in which these fluxes were not suppressed and the differences turned out to be slight.

Guided by results from the coupled boundary layer air-sea transfer experiment (CBLAST: see Black *et al.* 2007, Drennan *et al.* 2007, French *et al.* 2007, Zhang *et al.* 2008) and as in Smith *et al.* (2014b), the drag coefficient C_D is determined by the formula

$$C_D = [(0.7 + 1.4\{(1 - exp(-0.055R_F\,|\mathbf{u_b}|)\}] \times 10^{-3}, \tag{10}$$

where $R_F = 0.8$ reduces the boundary layer wind speed, $|\mathbf{u_b}|$, to the 10-m level. In contrast, C_K is set to a constant value of 1.3×10^{-3}.

When the equations are discretized in the vertical, the surface fluxes of heat and momentum enter the equations for the boundary layer through the D-terms as follows. The contributions of the frictional drag terms to D_u and D_v in Equations 1 and 2 are obtained by dividing the corresponding terms F_u and F_v in Equation 9 by the depth z_b and the density ρ_b of the lower layer. Dividing F_{sh} by $(\rho_b c_p \pi_s z_b)$ and F_q by $(\rho_b z_b)$ gives the contributions of the surface fluxes of sensible and latent heat to D_θ and D_q, respectively.

2.2.2. Subgrid-scale diffusion

To suppress small-scale noise and numerical instability in the model, it is necessary to filter out energy in high-frequency waves. In an axisymmetric model, the parameterization of subgrid-scale diffusion not only represents unresolved subgrid-scale motions. Any non-axisymmetric motion such as mesovortices in the eye or eyewall, boundary layer roll vortices, upper-level asymmetric outflow jets, or vortex Rossby waves must be viewed as turbulence in an axisymmetric model, and hence,

must be incorporated through parameterization (Bryan and Rotunno 2009). Thus, as in the asymmetric version of the model, a biharmonic damping term is appended to all prognostic equations except the pressure tendency equation. This term has the form

$$- k_4 \nabla^4 \chi, \tag{11}$$

where χ is any of the variables u, v, θ, q, and k_4 is a diffusion coefficient with $k_4 = \Delta^4/\tau_4$, where Δ is the horizontal grid spacing, and τ_4 is a time scale, set here to 0.0625 hours. Contrary to Nguyen *et al.* (2002), we found that the biharmonic damping term *is* sufficient to smear out large amplitude shocks that occur at grid points where there is a sudden release of latent heat associated with the explicit condensation on the grid scale.

In addition to biharmonic damping, Newtonian damping terms of the form $-\nu u$ and $-\nu v$ are added to the momentum equations for u and v in the outermost quarter of the domain in order to diminish the reflection of disturbances that reach the outer boundary. The damping coefficient increases with radius according to

$$\nu = \frac{1}{2\tau_1}\left[1 - cos\left(\pi\frac{r - r_d}{R - r_d}\right)\right], \tag{12}$$

where r_d is the radius at which the Newtonian damping term is first applied, R is the domain size in the radial direction, and τ_1 is a time scale set to 360 s. In regions of the flow which are anticyclonic, this term provides a source of angular momentum, while in regions where the flow is cyclonic, it represents a sink of angular momentum.

2.3. Parameterization of convection and explicit moist processes

Latent heat release in deep cumulus clouds on the subgrid-scale is represented by a parameterization scheme proposed by Arakawa (1969). The scheme is a type of mass flux scheme in which the subgrid-scale mass flux is determined by assuming that deep convection tends to remove any conditional instability on a prescribed time scale. This time scale is typically on the order of an hour, a value that is used for this study. The removal of instability is accomplished by relaxing the moist static energy of the upper layer towards that of the boundary layer on the assumed time scale. This scheme is complemented by a simple explicit scheme that is implemented where there is condensation on the grid scale. The two schemes are largely complementary in the sense that once a grid column saturates, the convection parameterization scheme tends to turn off in that grid column. See Zhu *et al.* (2001) for further details of these schemes.

2.4. Parameterization of radiative cooling

The effect of radiative cooling is crudely represented by the Newtonian cooling term, $R_\theta = -(\theta - \theta_{ref})/\tau_R$ to the right-hand-side of the thermodynamic equation, Equation (6). Here, θ_{ref} denotes the potential temperature profile of the basic state and τ_R is a radiative time scale. Following Mapes and Zuidema (1996), this time scale is set to 10 days. As in previous versions of the model, the cooling rates were capped at -2K d^{-1} although this rate is rarely exceeded with the new 10 day time scale. In earlier calculations with

the model, where, following Rotunno and Emanuel (1987, p546), τ_R was set to 12 h, this capping was essential to prevent unrealistic large cooling rates in the central region. In the present model, relaxation was not applied when the relative humidity in the upper layer exceeded 90 % as a crude way of representing the effect of cloud cover on the heat lost to space by radiation. A similar relaxation term, $R_q = -(q - q_{ref})/\tau_R$ is applied to the moisture tendency beyond a radius of 500 km to suppress moisture changes in the far field.

2.5. *Boundary and initial conditions*

The calculations are carried out in a cylindrical domain $(0 \leq r \leq R, 0 \leq \sigma \leq 1)$, with $R = 3000$ km. The boundary conditions in each layer at $r = 0$ and $r = R$ are:

$$u = 0, v = 0, \frac{\partial A}{\partial r} = 0, \qquad (13)$$

where A can be any of the quantities u, v, θ, q.

The initial tangential wind profile is that used by Nguyen *et al.* (2008), which has a maximum tangential wind speed of 15 m s^{-1} at the surface at a radius of 100 km. The balanced temperature field corresponding with this vortex is obtained using the method described by Smith (2006: see section 2.3 therein). The far-field temperature and humidity structure are based on the Dunion tropical sounding (Dunion 2011). The initial surface pressure is 1015.1 mb. In the presence of the initial vortex, the minimum surface pressure (at the vortex centre) is 1009 mb.

2.6. *Numerical method*

The model has three layers of unequal depth with boundaries at $\sigma = 1, \sigma_4, \sigma_2$ and $\sigma = 0$ as depicted in Fig. 1. All dependent variables, such as horizontal velocity, potential temperature, specific humidity and geopotential, are defined in the middle of each layer ($\sigma = \sigma_b, \sigma_3$, and σ_1) and the vertical velocity is staggered, *i.e.* it is defined at the boundaries between the layers ($\sigma = \sigma_4$ and σ_2). In the radial direction, the horizontal velocity components, u and v, are staggered also as indicated in Fig. 1. This is the so-called Lorenz-grid (L-grid). The advantage of the L-grid model is that total energy is conserved. In addition, the mean potential temperature and the variance of the potential temperature are conserved under adiabatic and frictionless processes (Arakawa and Suarez 1983).

A disadvantage of using the L-grid is that it permits a computational mode and in the study by Zhu and Smith (2003) it was replaced by a Charney-Phillips grid. At that time it was thought that the subsequent flow evolution should be approximately symmetric and Zhu and Smith (2003) found that this was much more the case when using the Charney-Phillips grid. Subsequently, it was recognized that the development of flow asymmetries were a natural consequence of the development of resolved-scale deep convection in the model (Shin and Smith 2008, Nguyen *et al.* 2008) rather than a negative consequence of using the L-grid. In this study we adopt the L-grid for its conservation properties in long-term integrations. The equations are expressed in finite difference form in both the radial and vertical and integrated using the Adams-Bashforth third-order method with an integration time step of 6 s.
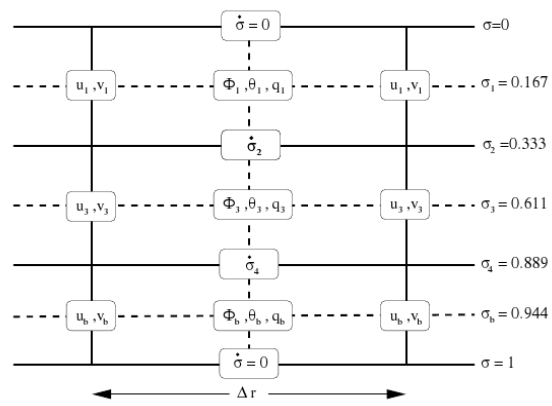
Figure 1. Configuration of σ-levels in the model with a Lorenz grid showing locations where the dependent variables are stored. The horizontal velocity components, geopotential, temperature, specific humidity are calculated in the middle of each layer. These are the layers 1, 3 and b. The vertical velocity $\dot{\sigma}$ and the convective mass fluxes are stored at the two interface levels 2 and 4. From Nguyen *et al.* (2002).

3. The calculations

In order to address the issues/questions posed in the introduction, we present one calculation that investigates the evolution of an initially weak baroclinic vortex to a mature tropical cyclone and the subsequent decay of this cyclone over a 20 day period. The Coriolis parameter, f, is set to a constant value, f_o, that corresponds to a reference latitude of 20°N.

4. Paradigm for understanding the results

To provide a setting for an interpretation of the results, we review briefly the azimuthally-averaged view (relevant here) of the rotating convection paradigm for intensification articulated by Montgomery and Smith (2014) and Smith and Montgomery (2015). In the classical mechanism for intensification, which Montgomery and Smith *op. cit.* term "the cooperative intensification paradigm", the spin up of the winds above the boundary layer (that are widely held to be in approximate gradient wind balance) is accomplished by the convectively-induced inward radial advection of the surfaces of constant absolute angular momentum[†], M, where this quantity is approximately materially conserved. It is assumed that surface moisture fluxes are sufficient to maintain the required deep convective activity.

It turns out, however, that the spin up of the maximum tangential winds takes place within the frictional boundary layer, where M is not materially conserved and where the winds are no longer in approximate gradient wind balance. While at first sight this idea may seem counter intuitive, it has a simple explanation. What happens is as follows. The breakdown of gradient wind balance by the frictional retardation of the tangential wind component leads to a net inward (agradient) force in the boundary layer, which, as it turns out, leads to a much stronger inflow than in the vortex above. The stronger the inflow, the shorter is the trajectory of air parcels as they spiral inwards and therefore the smaller is the loss of M caused by the frictional torque. Spin

---

[†]The quantity M is defined in terms of the tangential wind speed v by the formula $M = rv + \frac{1}{2}fr^2$, where r is the radius and f is the Coriolis parameter. Alternatively, $v = M/r - \frac{1}{2}fr$.

Copyright © 2015 Royal Meteorological Society

Prepared using qjrms4.cls

Q. J. R. Meteorol. Soc. **00**: 1–14 (2015)

up of the maximum tangential winds in the boundary layer is possible if the fractional rate of reduction of M fo;;owing an air parcel is less than the fractional rate of reduction of inward displacement of the air parcel. Following the foregoing authors, we refer to this feature as "the boundary-layer spin up mechanism".

(a)

(b)

(c)
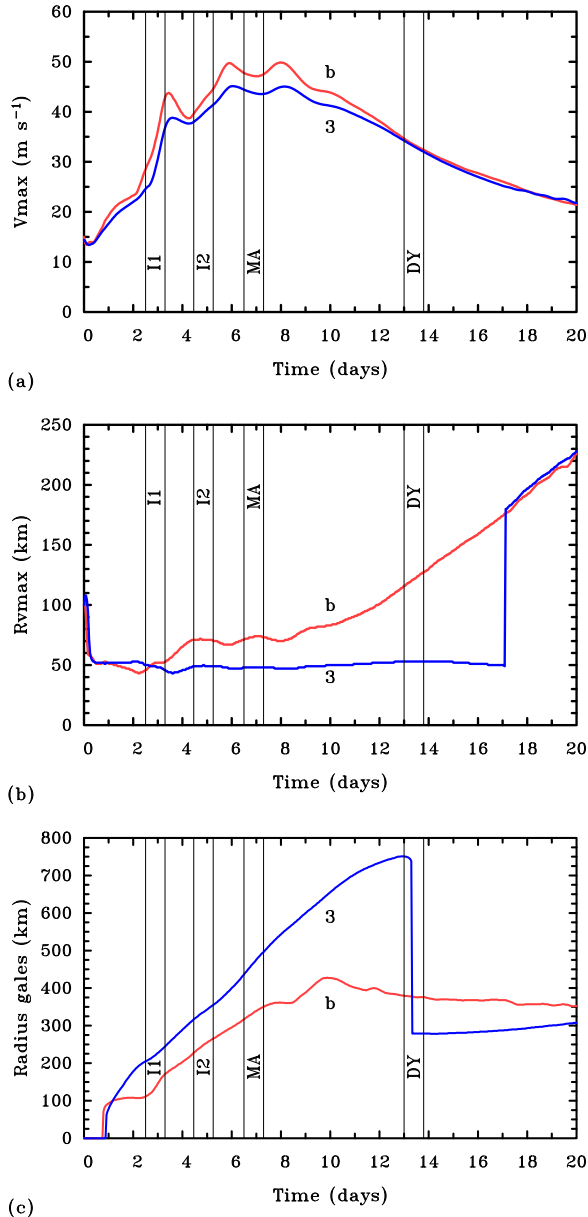
Figure 2. Time-series of (a) maximum tangential wind speed, V_{max} and (b) the radius, R_{vmax}, where it occurs. Panel (c) shows the outermost radius of gale-force winds, R_{gales}. The red curves are for the boundary layer, labelled b, the blue curves for the middle layer, labelled 3. The vertical lines in each panel delineate four periods of evolution depending on V_{max}. The intervals I1 and I2 refer to two periods of rapid intensification, MA refers to the mature stage and DY refers to the decay phase. The jumps in R_{vmax} and R_{gales} in panels (b) and (c) are associated with the development of new local maxima of V_{max} in the middle layer as discussed in the text.

The two mechanisms of spin up are coupled through boundary layer dynamics. Moreover, because the strength of both wind components in the boundary layer increases as the tangential wind speed above the boundary layer increases, a spin up of the winds in the boundary layer requires a spin up of the winds above the boundary layer as well.

In the absence of deep convection, the inflow within the frictional boundary layer leads to outflow just above the boundary layer and therefore spin down on account of the outward advection of the M-surfaces. Clearly, for the vortex above the boundary layer to spin up, the inner-core convection must be strong enough to reverse the effect of friction and produce inflow above the boundary layer. In other words, this convection must be strong enough not only to "ventilate" the air that is converging in the boundary layer, but also to draw air inwards in the lower troposphere, at least beyond a certain radius (see section 6.5).

5. Results: control experiment

5.1. Evolution of intensity

Figure 2 shows time series of the maximum tangential wind speed, V_{max}, in the lower and middle layers together with the radii, R_{vmax}, where they occur. It shows also the radii, R_{gales}, at which the tangential wind speed in the lower and middle layers fall to gale force (17 m s^{-1}). During the first few hours the vortex slowly decays due to surface friction (see section 4). Thereafter, as convective heating commences, the vortex begins to intensify. After about 2 days the vortex undergoes rapid intensification (RI) (the period I1 in Fig. 2), then decays a little before reintensifying (the period I2 in Fig. 2) to reach a peak intensity of 49.7 m s^{-1} in the lower layer after about 5 and a half days. After reaching its peak intensity, the vortex undergoes a further period of slight decay followed by a re-intensification phase before steadily decaying. At the end of the simulation, V_{max} is 21.4 m s^{-1}. Shown in Fig. 2 are two other periods characterizing the mature phase (MA) and decaying phase (DY), which will be referred to later.

Note that the maximum tangential wind speed in the middle layer is always smaller than that in the lower layer with maximum differences of about 5 m s^{-1} at times where the intensity has a local maximum.
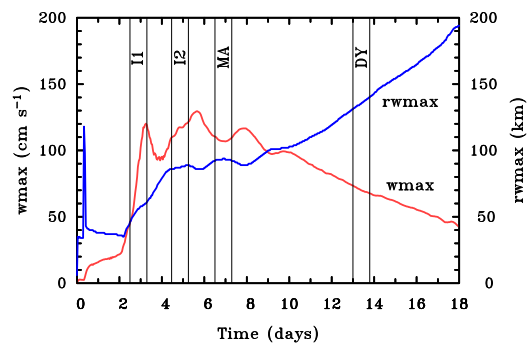
Figure 3. Time-series of maximum vertical velocity from the middle to the upper layer and the radius, R_{wmax}, where it occurs. The periods I1, I2, MA and DY are as defined as in Fig. 2.

5.2. Evolution of inner-core vortex size

The radius of maximum tangential wind speed, R_{vmax} serves as a metric for the inner-core size. Figure 2b shows time series of this metric. The onset of rapid intensification after 2 days coincides with the lowest value of R_{vmax} of 43 km in the lower layer. Thus, in this layer, the inner-core size increases *even during the period of rapid intensification*. Thereafter, R_{vmax} steadily increases.

In the middle layer, the minimum R_{vmax}, about 44 km, occurs just after the first period of RI and its value remains quasi-steady until about 17 days. The longer term behaviour of R_{vmax} in this layer requires some clarification. In section 5.6, we show, *inter alia*, Hovmöller plots of v. These plots indicate that beyond about 13 days, the tangential wind field develops two local maxima, first in the lower layer and a few days later in the middle layer. The first local maximum is found at about 50 km in both layers and its location remains steady for the entire simulation. However, the second local maximum increases in magnitude, eventually exceeding that of the first maximum. The curve for R_{vmax} in Figure 2b follows the outer maximum. A study of the absolute angular momentum budget presented in section 6 will help to understand this aspect of vortex behaviour.

5.3. Evolution of outer-core vortex size

Figure 2c shows time series of the outermost radius of gale-force tangential wind speed, R_{gales}, which is used here to characterize the outer-core vortex size. Comparison with Fig. 2b shows that the evolution of R_{gales} is not obviously related to that of R_{vmax}, nor is it related to the evolution of V_{max}. This behaviour is in line with the observations of typhoons described by Weatherford and Gray (1988) that inner-core changes in the azimuthal-mean tangential wind speed often occur independently from those in the outer core.

In the lower layer, gale-force tangential wind speeds develop first at $r = 70$ km after a little under one day. Over the next 12 h, R_{gales} increases only slightly before levelling off. After about two and a half days, at the start of RI as delineated by I1, R_{gales} increases steadily, reaching a peak value of about 400 km after 10 days. At this time, V_{max} has already begun to decline. Thereafter, R_{gales} decreases to a value of 350 km after 20 days.

In the middle layer, R_{gales} progressively increases, reaching a peak value of about 750 km just after 13 days. Then, the value falls abruptly to a quasi-steady value of 280 km. The reason for this behaviour is discussed in section 5.6).

5.4. Comparison to Kilroy et al. (2015)

In a similar calculation to the one here, but using a more sophisticated multi-layer model, Kilroy *et al.* (2015) showed that during a 30 day integration, the tropical cyclone grew progressively in size and decayed in intensity after reaching maturity. The behaviour of the vortex in our simulation is quite similar, although the decay after reaching maturity is more rapid, the growth in R_{vmax} during the decay phase is larger, but the growth in R_{gales} does not continue (Fig. 2). A likely reason why R_{gales} does not expand throughout the whole simulation as in the calculation by *et al.*, but starts to contract again after about 10 days is that V_{max} in the Kilroy *et al.* simulation still lies above hurricane-strength after 30 days of integration, while the final intensity in our calculation has dropped as low as 21.4 m s^{-1} after 20 days. The inner-core vortex size, as measured by R_{vmax}, increases progressively thoughout the whole simulation and reaches unrealistic values on the order of 200 km after 20 days, whereas that in the Kilroy *et al.* simulation it increases only to about 70 km. However, unlike in their simulation, the tangential wind field in the present one develops two local maxima (Fig. 2b). This

development is not akin to an eyewall replacement cycle as the outer maximum moves outwards with time. At this stage, we do not have an explanation for all these differences in detail.

5.5. Evolution of the secondary circulation

Figure 3 shows time series of the maximum vertical velocity, w_{max}, from the middle to the upper layer. This quantity is a measure of the strength of the secondary circulation. Shown also is a time series of the radius R_{wmax}, at which w_{max} occurs. As the storm intensifies, R_{wmax} provides information about the location of the eyewall updraught. The temporal evolution of these quantities follows those of V_{max} and R_{vmax}, respectively (compare Figs. 2a,b with Fig. 3). The maximum value for w_{max} of 129 cm s^{-1} occurs at about five and a half days, where the time series of V_{max} shows its peak maximum. We do not show values of w_{max} beyond 18 days when the vertical velocity becomes very small and its radial distribution shows several local maxima.

While w_{max} is one measure of the strength of the secondary circulation passing through the eyewall updraught, it is not the key measure. This is because it does not quantify the ability of this updraught to ventilate the mass converging in the boundary layer. What matters for generating inflow above the boundary layer to spin up the tangential winds (the classical spin up mechanism discussed in section 4) is the difference between the radially-integrated mass flux across the updraught at the top of the middle layer and that at the top of the lower layer, i.e. the top of the boundary layer. We denote this difference by dMf. Specifically, the mass fluxes, themselves, are calculated by integrating the vertical velocity, where it is positive, with respect to radius and multiplying by the ambient density at each level. The integration extends to a radius, $R_{MF} = 150$ km, large enough to encapsulate the eyewall updraught, but small enough that the neglect of negative values of vertical velocity is justified.

Figure 4 shows a time series of dMf together with a time series of V_{max} in the middle layer. Positive values of dMf indicate that the eyewall updraught is more than able to ventilate the mass flux expelled from the boundary layer so that, by mass continuity, there must be inflow in the middle layer at and beyond $r = R_{MF}$. Such inflow is indeed found during this period as shown in Fig 5d. Assuming the material conservation of absolute angular momentum in this layer, this inflow would lead to a spin up of the tangential wind there. In contrast, negative values of dMf imply that not all of the air that leaves the boundary layer can be vented into the upper troposphere within the eyewall so that there must be radial outflow at $r = R_{MF}$ and an accompanying tendency to spin down of the tangential winds in the middle layer there.

During the first few hours of the simulation, V_{max} decreases slightly in the middle layer and, as expected, dMf is negative during the time period. During the subsequent gradual increase in intensity, dMf becomes positive, again as expected. However, during the rapid intensification phase after two days, dMf again becomes negative, contrary to expectations based on the foregoing considerations and there must be another process by which the inner-core tangential winds spin up in the middle layer. As will be shown in section 6, the spin up of the eyewall region occurs by the vertical advection of angular
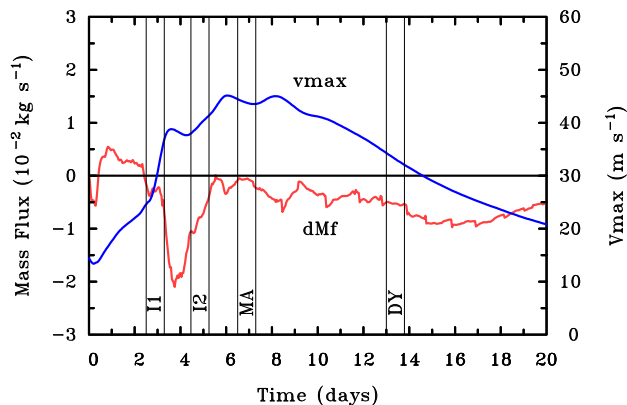
Figure 4. Time series of the difference between the mass fluxes at the upper and the lower level, dMf (red contour) and the maximum tangential wind speed in the middle layer (blue curve). The periods I1, I2, MA and DY are as defined as in Fig. 2.

momentum from the boundary layer and not by the classical spin up mechanism .

Beyond the onset of the first rapid intensification phase, dMF is generally negative, which would imply outflow at $r = R_{MF}$. It turns out that there is outflow in the middle layer within this radius (see Fig. 5d) suggesting that any spin up there must be associated with the vertical advection of angular momentum from the boundary layer. This inference will be affirmed in section 6.

5.6. Evolution of vortex structure

Further insight into the evolution of vortex structure is provided by time-radius plots of various quantities shown below.

Figure 5 shows time-radius plots of the tangential and radial wind speed components in each of the three layers. Similar plots of vertical velocity at the two interface levels, relative humidity in the middle and lower layers, and surface sensible and latent heat fluxes are shown in Fig. 6. During the first 51 h, the vortex intensity increases gradually in all three layers, while the radius of maximum tangential wind speed decreases. For example, in the boundary layer, R_{vmax} decreases from 100 km to about 50 km. The strong moisture fluxes at the sea surface that typically increase with wind speed and with decreasing pressure[‡] lead to rapid saturation of the lower layer (in a vertical mean sense) after only three hours (see Fig. 6c). Of course, in reality, this tendency for the boundary layer to saturate would be opposed by vertical mixing through the top of the layer by processes involving shallow convection, which are not represented in the present model.

The moistening of the inner core in the middle layer occurs by vertical advection from below. However, even prior to the occurrence of grid-scale saturation in the middle layer after 51 h, subgrid-scale deep convection leads to slight warming of the inner core. This warming leads to a moderate strength secondary circulation with low- and middle-level convergence, ascent near the radius of maximum tangential wind speed and divergence aloft (see right panels of Figures 5 and 6). The onset of RI at 51 h occurs when there is grid-scale saturation in the inner core of the middle layer (Fig. 6a). The explicit release of latent

heat leads to a sudden increase in the radial gradient of diabatic heating, which, in turn leads to a sharp increase in the strength of the secondary circulation, *i.e.* strong convergence in the lower and middle layers, strong ascent at both interface levels and divergence in the upper layer (Fig. 5b,d,f and Fig. 6c,d). The convective parameterization scheme becomes inactive at radii less than about 150 km after 60 hours and at all radii after about 4 days.

The annular region of strong ascent depicted in the right panels of Fig. 6 is accompanied by subsidence near the centre, indicative of an eye. Even prior to rapid intensification, a region of strong subsidence has formed. After about three days, however, the region of strongest subsidence is found just inside the ascent region of the eyewall whereas the air at the centre is slowly ascending. This behaviour has been described in an analytical study by Schubert *et al.* (2007). Another prominent feature of the vortex evolution is the development of an upper-level anticyclone at outer radii after about half a day (see section 5.7).

With the onset of RI, the vertical velocity fields show also regions of strong subsidence outside the inner-core region (the region outside the "eyewall updraught"), which account for adiabatic warming and drying in the middle and lower layers. The subsidence advects also lower values of absolute angular momentum from the upper layer into the middle layer, which accounts for the development of a local minimum in the tangential wind field after about 6 days (see Fig. 5c). The sudden collapse of R_{gales} from 750 km to 280 km after 13 days seen in Fig. 5c can be attributed to this downward advection process. A study of terms in the tangential momentum equation presented in section 6 sheds further light into this feature.

During the course of this work we discovered that the surface fluxes of sensible and latent heat in calculations with earlier versions of the present model were unrealistically large. This feature was found to occur because of the assumption of a well-mixed boundary layer as is made in the Emanuel formulations (Emanuel 1989, 1997, 2003, 2012). To remedy this problem we modified the parameterization scheme for the surface enthalpy fluxes as detailed in section 2.2.1. Time-radius plots of surface sensible and latent heat fluxes in the present calculation are shown in the lower panels of Fig. 6. Both fluxes increase strongly with wind speed in the inner core and reach maximum values of about 240 W m^2 and 1380 W m^2, respectively. Using the modified scheme, the maximum values of sensible and latent heat fluxes and the radial distribution of the Bowen ratio compare reasonably well with those in an observational study by Cione *et al.* (2000).

5.7. Outflow layer, upper anticyclone

Figure 7 shows time series of the minimum tangential wind speed in the upper layer and the radius, R_{vmin}, where it occurs. The upper anticyclone begins to develop after half a day of simulation. The minimum tangential wind speed decreases monotonically to -42.9 m s^{-1} and the radius, where it occurs increases steadily to 1540 km after 20 days. The upper anticyclone continues to grow throughout the simulation and over the 20 days of integration, the vortex does not reach a globally steady-state.

[‡]See Eq. (9) and recall that q_s^* increases with decreasing surface pressure.
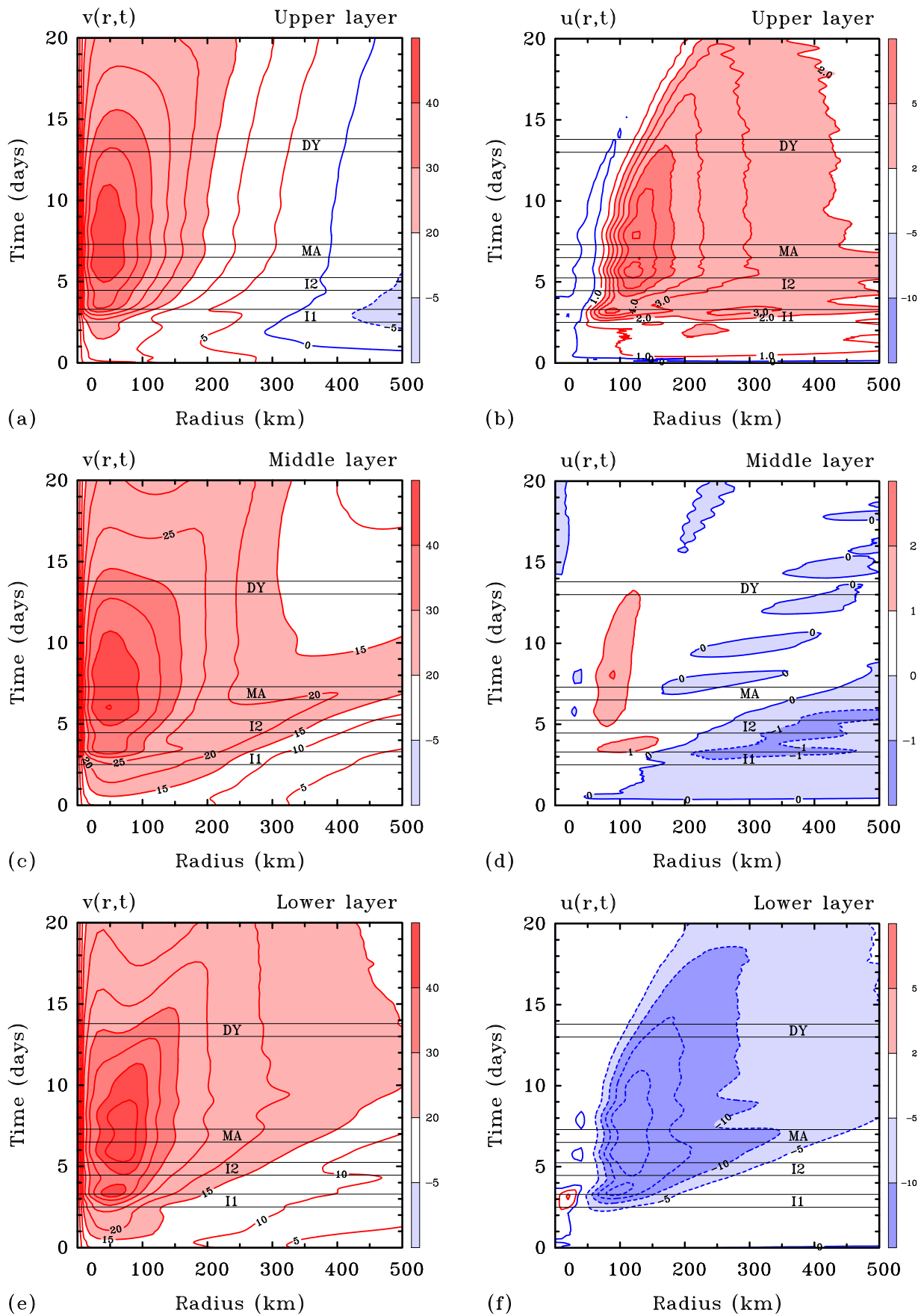
Figure 5. Time-radius plots of the tangential, v, and radial wind speed components, u. Positive values red/solid, negative values blue/dashed. (a) v in the upper layer (contour interval is 5 m s^{-1}), (b) u in the upper layer (contour interval is 1.0 m s^{-1}), (c) v in the middle layer (contour interval as in panel a), (d) u in the middle layer (contour interval as in panel b), (e) v in the lower layer (contour interval as in panel a), (f) u in the lower layer (contour interval is 5 m s^{-1} (negative values) and 1 m s^{-1} (positive values)). The periods I1, I2, MA and DY are as defined as in Fig. 2.
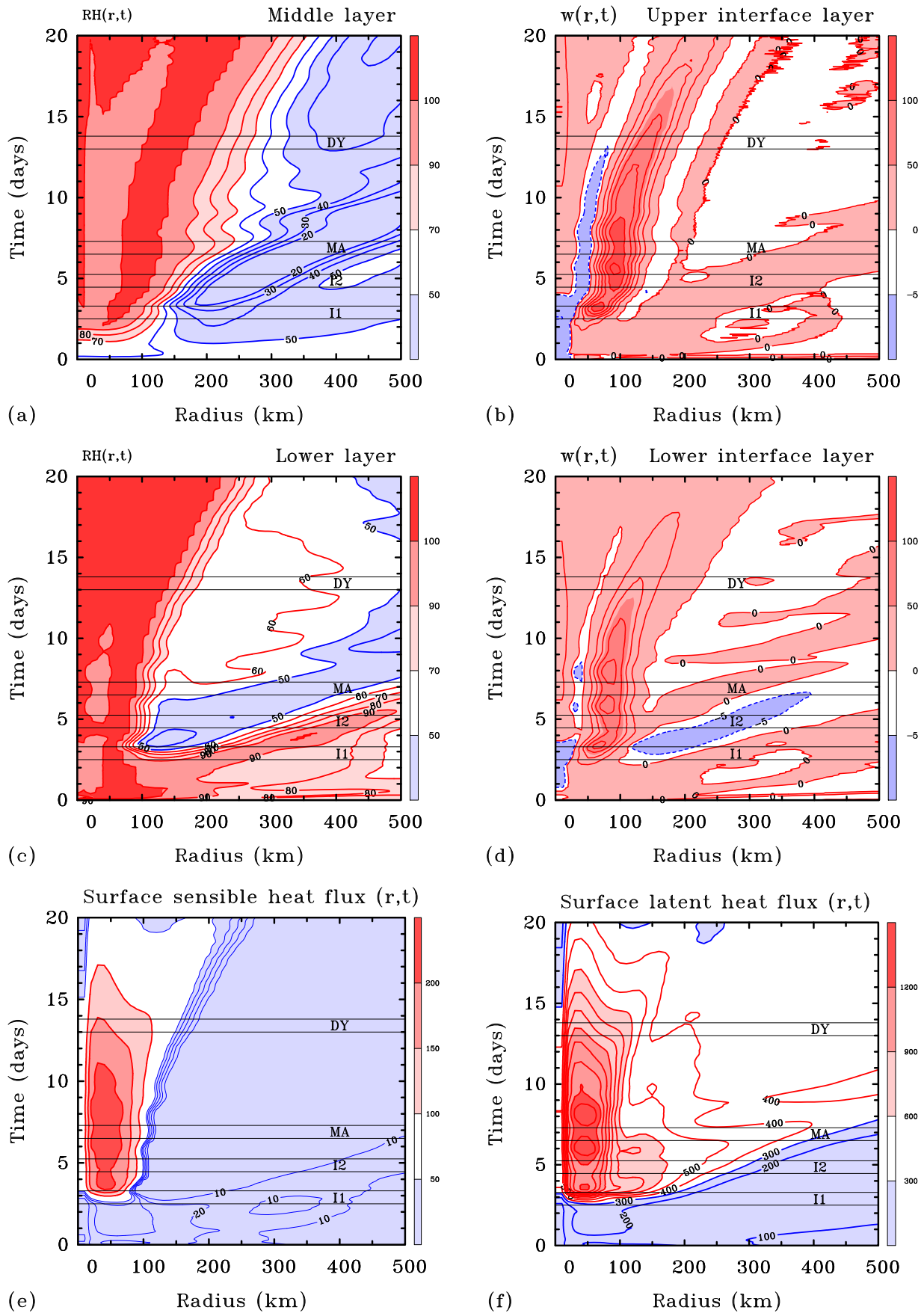
Figure 6. Time-radius plots of: relative humidity, RH, in (a) the middle layer and (c) the boundary layer; vertical velocity, w, at (b) the upper interface level, and (d) the lower interface level; (e) surface sensible heat flux and (f) surface latent heat flux. Contour interval for relative humidity is 10%. Positive contour interval vertical velocity is 20 cm s^{-1}, the negative contour is -5 cm s^{-1}. Contour interval for the heat fluxes is 10 W m^{-2} in panel (e) and 100 W m^{-2} in panel (f). The periods I1, I2, MA and DY are as defined as in Fig. 2.

Prepared using qjrms4.cls

Q. J. R. Meteorol. Soc. **00**: 1–14 (2015)

6. Discussion and further interpretation

In this section we examine several important features of vortex evolution including: the boundary layer spin-up mechanism; the tangential momentum budget for the intensification and decay periods; the (artificial) source of cyclonic angular momentum resulting from the damping of tangential momentum in the far field; and finally the ventilation of the boundary layer inflow.
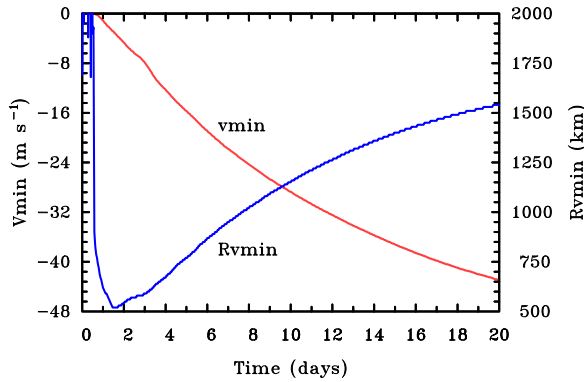
Figure 7. Time-series of minimum tangential wind speed, V_{min} in the upper layer and the radius, R_{vmin}, where it occurs.

6.1. Spin up in the boundary layer

To illustrate the boundary-layer spin up mechanism, we show in Fig. 8 time-radius plot of the difference, $dv = v_b - v_3$, between the tangential wind speed component in the boundary layer and the middle layer together with the agradient force in these two layers. In contrast to Figs. 5-6, Fig. 8 shows the evolution for the first eight days covering the intensification and mature phases of the vortex. The agradient force (per unit mass), F_a, is defined as the difference between the local pressure gradient force and the sum of the centrifugal and Coriolis forces (per unit mass), i.e. $F_a = -(1/\rho)(\partial p/\partial r) + (v^2/r + fv)$. The tangential flow is in exact gradient-wind balance if $F_a = 0$. If $F_a < 0$, the flow is *subgradient* and if $F_a > 0$, it is *supergradient*. Consistent with the explanation in section 4, there is a range of radii near or inside R_{vmax} in which the tangential wind speed in the boundary layer is larger than above (Fig. 8a).

The behaviour in Fig. 8 is consistent with the description in section 4. At early times, $v_b > v_3$ because the initial tangential wind speed decreases with height (Fig. 8a), but the boundary layer becomes subgradient (except in localized regions that are indicative of inertia-gravity waves generated by the sudden imposition of friction) as seen in Fig. 8c. After about a day, the flow in the boundary layer becomes strongly subgradient beyond a radius of about 50 km. The negative agradient force accelerates air parcels rapidly inwards in this layer (Fig. 5f), with only modest loss of absolute angular momentum so that the flow becomes supergradient in a 20-30 km wide region inside this radius. The inflow then decelerates and turns upwards. Note that the region of supergradient winds coincides with the region of strong ascent from the boundary layer into the eyewall updraught. This region is indicated by the thick black line that depicts the 20 cm s^{-1} contour of vertical velocity at the top of the boundary layer in Fig. 8b and 8c.

Values of F_a in the middle layer are much smaller than those in the boundary layer (Fig. 8c), so that, especially
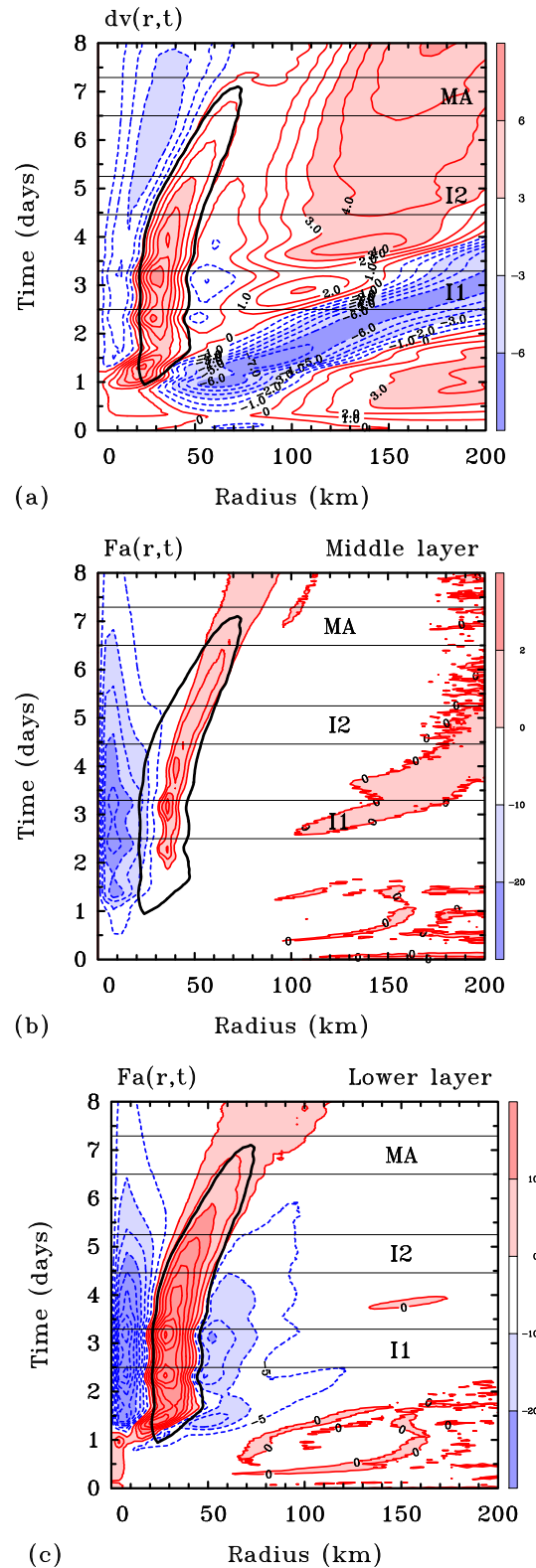
Figure 8. Time-radius plots of (a) the difference between the tangential wind speed in the boundary layer and the middle layer (contour interval 1 m s^{-1}, positive contours red/solid, negative contours blue/dashed). Shown also is the agradient force in (b) the middle layer (contour interval 1 m s^{-1} h^{-1} (positive values), 5 m s^{-1} h^{-1} (negative values)) and (c) boundary layer (contour interval 5 m s^{-1} h^{-1}). Positive contous red/solid, negative contours blue/dashed. The thick black curve in each panel is the 20 cm s^{-1} contour of vertical velocity from the boundary layer to the middle layer in the eyewall region.

outside some inner-core region, gradient wind balance serves as a good approximation. The positive values of F_a

Prepared using qjrms4.cls

within the updraught drives outflow (see Fig. 5d) that leads to a spin down of the layer and thereby to a readjustment back to gradient wind balance.

6.2. Tangential momentum budget

In order to understand some details of the spin-up and decay processes in the model we investigate now the magnitude of each of the terms in the tangential momentum equation (Equation 2). First, it may be helpful to recall different forms of the tangential momentum equation. With a few lines of algebra, it can be shown, that these three equations are equivalent:

$$\frac{\partial v}{\partial t} = -u\frac{\partial v}{\partial r} - \dot{\sigma}\frac{\partial v}{\partial \sigma} - fu - \frac{uv}{r} + D_v, \qquad (14)$$

$$\frac{\partial v}{\partial t} = -u(\zeta + f) - \dot{\sigma}\frac{\partial v}{\partial \sigma} + D_v, \qquad (15)$$

$$\frac{1}{r}\frac{\partial M}{\partial t} = -\frac{u}{r}\frac{\partial M}{\partial r} - \frac{\dot{\sigma}}{r}\frac{\partial M}{\partial \sigma} + \frac{D_v}{r}, \qquad (16)$$

where $\zeta = (1/r)(\partial(rv)/\partial r)$ is the vertical component of relative vorticity in the model coordinates. All other variables have been defined in section 2. These equations show that the sum of terms $-u\partial v/\partial r - uv/r - fu$ in Equation 14 is equivalent to the radial flux of absolute vorticity, $-u(\zeta + f)$ in Equation 15, and to the radial advection of absolute angular momentum divided by r, i.e. $-(u/r)(\partial M/\partial r)$ in Equation (16). The latter equation shows that in regions where diffusion is negligible, typically above the boundary layer, $DM/Dt = 0$ so that absolute angular momentum is materially conserved.

Figure 9 shows radial profiles of all contributions to the tangential momentum equation in all three layers during the first period of RI. Panel (c) shows that the vortex spin-up in the boundary layer occurs predominantly by the inward flux of absolute vorticity (equivalent to the inward advection of absolute angular momentum). Another positive contribution to $\partial v/\partial t$ is the vertical advection term with a magnitude that is less than half of that of $-u(\zeta + f)$.

In regions where $v_b > v_3$ and the flow is upwards, i.e. ($\dot{\sigma} < 0$), $-\dot{\sigma}\partial v_b/\partial \sigma$ is positive (see Fig. 8a). Significantly, the radial diffusion term is strongly negative between $r = 40$ and 80 km with a magnitude that is comparable with that of $-u(\zeta + f)$. Surface friction, a dominant term in the boundary layer, becomes very large also in the inner core on account of the high wind speed near the eyewall. Of course, the sum of all terms is positive during RI.

Panels (b) and (c) of Fig. 9 show that at radii less than 40 km, the spin-up tendency is dominated by the radial diffusion of tangential momentum from the eyewall, while at radii between 80 and 150 km, diffusion makes an important contribution to spin up also, both in the lower and middle layers. Since radial diffusion in the model is implemented principally to control numerical aliasing and has little physical basis, we resist making physical interpretations involving the role of radial diffusion, especially in an axisymmetric model. Indeed, more sophisticated three-dimensional simulations of tropical cyclone behaviour indicate that "eddy momentum transfer" is not even downgradient in the inner core region of the storm (Persing *et al.* 2013).

It is significant that the strong upward motion from the boundary layer to the middle layer occurs at radii where the tangential wind speed is largest in the boundary layer (see Fig. 8a). Thus, at these radii, the middle layer is being fed by angular-momentum enriched air. Figure 9b shows that, in the same annular region, there is an outward flux of absolute vorticity in the middle layer, equivalent to a negative advection of absolute angular momentum. By itself, this outward flux would lead to spin down of the tangential wind, but, as shown in Fig. 9b, the vertical advection of tangential momentum from the boundary layer dominates and the vortex spins up. Clearly, the spin-up of the middle layer in the updraught region is a result of the upward transfer of higher values of absolute angular momentum from the boundary layer and not from the radial advection of absolute angular momentum in the middle layer, supporting the ideas articulated by Nguyen *et al.* (2002), Smith *et al.* (2009) and Smith and Montgomery (2010). A similar behaviour is found in the second period of RI (I2, not shown).

It is worth pointing out that the foregoing process of spin-up cannot occur in time-dependent models that assume approximate gradient wind balance in the boundary layer such as those of Ooyama (1969), Emanuel (1997), Frisius (2006) and Wirth and Dunkerton (2006).

6.3. Source of cyclonic angular momentum

Figure 9a shows the tangential momentum budget in the outermost quarter of the domain, where Newtonian damping terms are added to the radial and tangential momentum equation in order to diminish the reflection of disturbances that reach the outer boundary (see section 2.2.2). It is seen that Newtonian damping is the dominant term beyond $r = 2250$ km and makes a positive contribution to spin up. While the damping terms are necessary for numerical reasons, the damping term in Eq. (14) represents an artificial source of cyclonic angular momentum as noted by Smith *et al.* (2014a). The subsequent decay of the vortex in the present calculations indicates that this source of cyclonic momentum is not large enough to maintain a globally steady state.

The foregoing finding prompted us to revisit the solutions presented in Smith *et al.* (2011) in which the solutions appeared to have become steady at least in terms of V_{max} and at least up to 12 days. Further examination of these solutions showed, however, that they were not globally steady at this time and, as in the case here, the upper anticyclone continues to evolve during the whole simulation.

It is perhaps worth pointing out that, in the present calculations, the Newtonian damping term only represents a *source* of angular momentum in the *upper* layer where the flow is anticyclonic. In the middle and lower layers, the flow is cyclonic everywhere whereupon Newtonian damping acts as a sink of angular momentum there.

6.4. Ventilation

Both during the first and second RI periods (I1 and I2) the radially-integrated vertical mass flux at the top of the middle layer is smaller than that at the top of the boundary layer (see Fig. 4). As discussed in section 5.5, in this situation, the eyewall updraught is not able to ventilate all the mass flux expelled from the boundary layer. Thus the air in the middle layer is constrained by mass continuity to move radially outwards in the updraught region, implying a spin
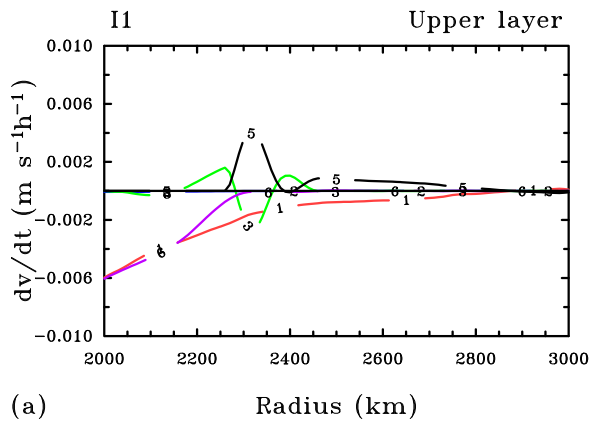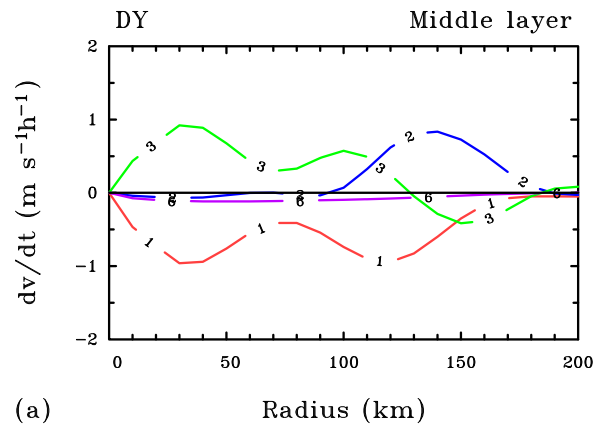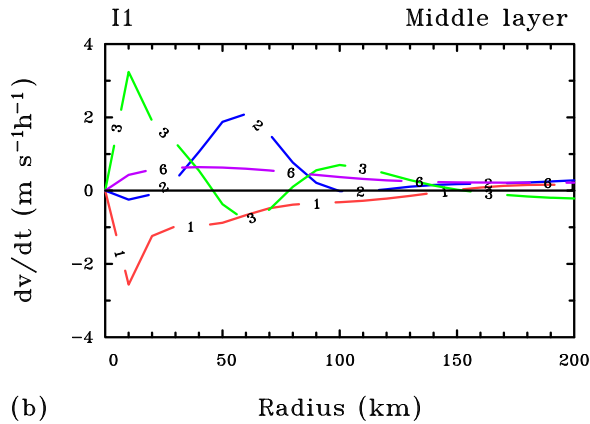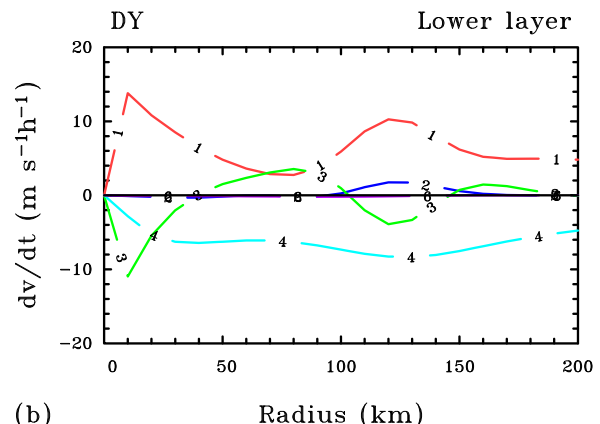
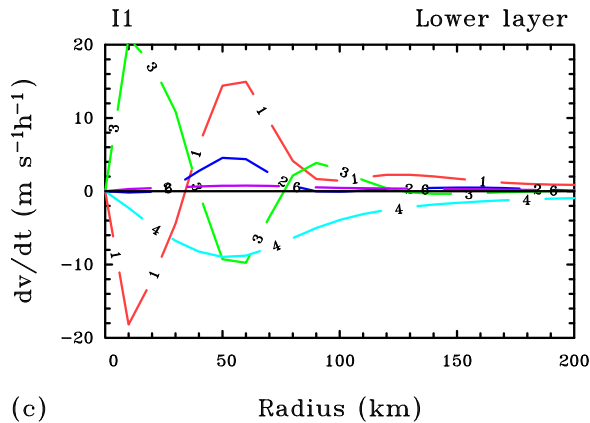**Figure 9.** Radial profiles of the contributions to the tangential momentum equation during period I1 (a) in the far field of the upper layer and in the inner-core region in (b) the middle layer and (c) the boundary layer. Curves 1 - 4 denote the contributions from the radial flux of absolute vorticity ($-u(\zeta + f)$, curve 1), vertical advection ($-\dot\sigma\partial v/\partial\sigma$, curve 2), contribution to D_v from radial diffusion (curve 3), and contribution to D_v from surface friction (curve 4). Curve 5 in panel a shows the contribution from the Newtonian damping term in the last quater of the domain. Curve 6 denotes the sum of all these terms, *i.e.* the tendency of v, $\partial v/\partial t$. Note the different scales in each panel.

Figure 10. Radial profiles of the contributions to the tangential momentum equation during the decay phase in the inner-core region of (a) the middle layer and (b) the boundary layer. Curves 1 - 4 denote the contributions from the radial flux of absolute vorticity ($-u(\zeta + f)$, curve 1), vertical advection ($-\dot\sigma\partial v/\partial\sigma$, curve 2), contribution to D_v from radial diffusion (curve 3), and contribution to D_v from surface friction (curve 4). Curve 6 denotes the sum of all these terms, *i.e.* the tendency of v, $\partial v/\partial t$. Note the different scales in each panel.

down tendency. However, the inner-core vortex spins up during this phase. We have shown above that the inner-core vortex in the middle layer during RI period I1 is spun up by the upward transfer of high of absolute angular momentum from the boundary layer and not by the inward flux of absolute vorticity. This spin-up mechanism occurs also during period I2 (not shown).

Figure 10 shows similar profiles to Fig. 9b and 9c during the decay phase. Surface friction has become the dominant term in the boundary layer and leads to gradual decay there. The contribution from the radial flux of absolute vorticity is still positive and shows two local maxima at about 10 and 120 km, which leads to a weaker decay rate between these radii and thus to the development of two local maxima in the tangential wind field of the boundary layer (see Fig. 5e). In the middle layer, spin-down occurs predominantly by the outward flux of absolute vorticity on account of conservation of absolute angular momentum. For radii between 100 and 180 km, the vertical advection term is still positive, although it is too small to outweigh the terms that contribute negatively to the absolute angular momentum budget. Nevertheless, the positive contribution from the vertical advection term to the angular momentum budget weakens the rate at which the vortex decays at these radii (see curve 6) and explains the development of two local maxima in the tangential wind field of the middle layer (see Fig. 5c).

6.5. Modified intensification paradigm

The foregoing results support the modified picture of vortex intensification shown in Fig. 13d of Montgomery and Smith (2014) and described in section 4. An important component of intensification is the formation of a region of supergradient winds in the inner-core boundary layer and the vertical advection of this high tangential momentum to spin up the air in the eyewall. The analyses presented in

section 6 highlight the dominance of this vertical advection in spinning up the eyewall, since in the minimal model, the radial flow in the eyewall updraught is outwards, even in the middle layer, and the radial advection of absolute angular momentum would lead there to spin down. Nevertheless, there is radial inflow in the middle layer somewhat outside the eyewall and this leads locally to spin up and thereby to an expansion of the outer tangential circulation (cf. Kilroy *et al.* 2015). As explained by Kilroy *et al.*, this expansion of the outer circulation can lead through boundary-layer dynamics to a further spin up of the inner-core winds in the boundary layer, which in turn would further spin up the eyewall. The proviso "can lead" is because, as explained in Kilroy *et al.*, the thermodynamic processes in the boundary layers must act favourably to support the intensification process. Figure 11 shows a schematic of the secondary circulation during the two RI phases in the current model based on the flow evolution shown in Figs. 5 and 6 together with the profiles of tangential wind tendency shown in Fig. 9.

The classical spin up mechanism associated with the radial inflow of absolute vorticity in the middle layer operates outside of the eyewall updraught (the region BC in the figure). In the eyewall region (the region AB), the spin up is associated entirely with the vertical advection of enhanced tangential momentum from the boundary layer. Here the radial flow in the middle layer is outwards so that the radial advection of absolute angular momentum makes a negative contribution to spin up. In a continuous model, the secondary circulation above the boundary layer is approximately along M-surfaces, which slope radially outwards with height. However, to have spin up, the flow must have a component across M-surfaces. Specifically, spin up requires that the M-surfaces move in a direction opposite to ∇M so that radial outflow, by itself, need not necessarily imply spin down[§]. In the three-layer model, the M-surfaces are, of course vertical in each layer so that outflow does imply a spin down tendency.
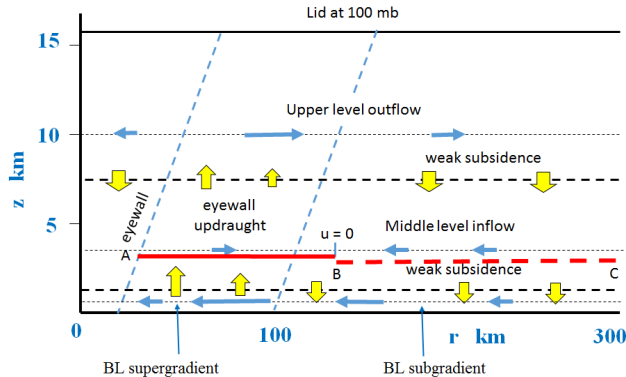
Figure 11. Schematic of the secondary circulation in the three layer model during the periods of rapid intensification. The heights of the different levels are only approximate, as these levels are sigma surfaces. The thick (yellow) arrows indicate the vertical velocity, the thin arrows the radial motion. The sloping dashed lines indicate the outward sloping boundaries of the eyewall updraught. The thick (red) horizontal lines AB and BC refer to the dominant spin up mechanism. See text for discussion.

[§] Spin up at a point requires simply that $\partial M/\partial t > 0$. In regions where M is materially conserved, this requirement becomes $-\mathbf{u_s} \cdot \nabla M > 0$, where $\mathbf{u_s}$ is the vector velocity of the secondary circulation, i.e. $\mathbf{u_s}$ must have a larger slope than the M-surface. This result follows from the vector form of Eq. (16) with $D_v = 0$.

7. Conclusions

We have developed an improved version of a minimal tropical cyclone model and used it to investigate some fundamental aspects of tropical cyclone behaviour. The improvements include a modified representation of surface enthalpy fluxes, making the fluxes more realistic in relation to recent observations. They include also a more realistic relaxation time scale for potential temperature and a modified horizontal diffusivity based on a biharmonic damping term. With these improvements, the vortex intensity did not become steady during a 20 day integration of the model. In fact, after going through a mature phase in which the maximum tangential wind speed remained quasi-steady for a few days, the vortex ultimately decayed. Even during the mature stage, the upper anticyclone continued to evolve and a global steady state was never achieved. This finding is consistent with recent studies using more sophisticated numerical models.

The calculation highlights the pivotal role of the boundary layer in spinning up the tangential winds in the eyewall updraught. The spin up in the boundary layer is associated with the development there of supergradient winds. The spin up of the eyewall updraught occurs by the vertical advection of the high tangential momentum associated with the supergradient winds in the boundary layer. These boundary layer and eyewall spin up mechanisms, while consistent with some recently reported results, are not part of the classical theory of spin up.

In the eyewall updraught, the flow is outwards (typifying the outward slope of the eyewall) so that the radial advection of absolute angular momentum (or radial flux of absolute vorticity) makes a negative contribution to spin up in this region. However, there is inflow in the middle layer at larger radii where the classical mechanism operates to spin up the tangential winds. Based on the results of Kilroy *et al.* (2015), the spin up at large radii, where the flow in the boundary layer is subgradient, may be expected to lead to a feedback on the inner-core vertical motion through boundary-layer dynamics.

While one cannot expect the minimal model to be realistic in every detail, we believe that the degree of realism makes it useful as a tool for investigating many fundamental aspects of tropical cyclone behaviour.

8. Acknowledgements

References

Anthes RA. 1972 Development of asymmetries in a three-dimensional numerical model of the tropical cyclone. *Mon. Wea. Rev.*, **100**, 461-476.

Arakawa A. 1969 Parameterization of cumulus convection. *Proc. WMO/IUGG Symp. Numerical Weather Prediction, Tokyo, 26 November - 4 December 1968, Japan Meteor. Agency IV*, **8**, 1-6.

Arakawa A Suarez MJ. 1983 Vertical differencing of the primitive equations in sigma coordinates. *Mon. Wea. Rev.*, **111**, 34-45.

Black PG D'Asoro EA Drennan WM French JR Niller PP Sanford TB Terril EJ Walsh EJ Zhang JA. 2007 Air-sea exchange in hurricanes: Synthesis of observations from the Coupled Boundary Layer Air-Sea Transfer Experiment. Bull. Amer. Meteor. Soc. **88**, 357-374.

Bryan GH Rotunno R. 2009 The maximum intensity of tropical cyclones in axisymmetric numerical model simulations. *Mon. Wea. Rev.*, **137**, 1770-1789.

Charney JG Eliassen A. 1964 On the growth of the hurricane depression. *J. Atmos. Sci.*, **21**, 68-75.

Cione JJ Black PG Houston SH. 2000 Surface observations in the hurricane environment. *Mon. Wea. Rev.*, **128**, 1550-1561.

Drennan WM Zhang JA French JR McCormick C Black PG. 2007 Turbulent fluxes in the hurricane boundary layer. Part I: Latent heat flux. *J. Atmos. Sci.*, **64**, 1103-1115.

Dunion JP. 2011 Rewriting the climatology of the tropical North Atlantic and Caribbean Sea atmosphere. *J. Clim*, **24**, 893-908.

Emanuel KA. 1989 The finite amplitude nature of tropical cyclogenesis. *J. Atmos. Sci.*, **46**, 3431-3456.

Emanuel KA. 1997 Some aspects of hurricane inner-core dynamics and energetics. *J. Atmos. Sci.*, **54**, 1014-1026.

Emanuel KA. (2003) Tropical Cyclones. *Annu. Rev. Earth Planet. Sci.*, **31**, pgs. 75 104.

Emanuel KA. (2012) Self-stratification of tropical cyclone outflow. Part II: Implications for storm intensification. *J. Atmos. Sci.*, **69**, 988-996.

French JR Drennan WM Zhang JA Black PG. 2007 Turbulent fluxes in the hurricane boundary layer. Part II: momentum fluxes. *J. Atmos. Sci.*, **64**, 1089-1102.

Frisius T. 2006 Surface-flux-induced tropical-cyclogenesis within an axisymmetric atmospheric balanced model. *Q. J. R. Meteor. Soc.*, **132**, 2603-2623.

Kilroy G, Smith RK, Montgomery MT. 2015 Why do model tropical cyclones grow progressively in size and decay in intensity after reaching maturity? *J. Atmos. Sci.*, **72**, in press.

Mapes BE, Zuidema P. 1996 Radiative-dynamical consequences of dry tongues in the tropical troposphere. *J. Atmos. Sci.*, **53**, 620-638.

Montgomery MT Smith RK. 2014 Paradigms for tropical-cyclone intensification. Australian Meteor. Ocean. Journl. (Bruce Morton Memorial Volume) **64**, 37-66.

Montgomery MT Zhang JA Smith RK. 2014 The low-level structure of rapidly intensifying and mature Hurricane Earl (2010). *Q. J. R. Meteor. Soc.*, **140**, 2132-2146.

Nguyen CM Smith RK Zhu H Ulrich W. 2002 A minimal axisymmetric hurricane model. *Q. J. R. Meteor. Soc.*, **128**, 2641-2661.

Nguyen SV Smith RK Montgomery MT. 2008 Tropical-cyclone intensification and predictability in three dimensions. *Q. J. R. Meteor. Soc.*, **134**, 563-582.

Ooyama KV. 1969 Numerical simulation of the life cycle of tropical cyclones. *J. Atmos. Sci.*, **26**, 3-40.

Persing, J Montgomery MT McWilliams J Smith RK. 2013 Asymmetric and axisymmetric dynamics of tropical cyclones, *Atmos. Chem. Phys.*, **13**, 12299-12341.

Rotunno R and Emanuel KA. 1987 An Air-Sea Interaction Theory for Tropical Cyclones. Part II: Evolutionary Study Using a Nonhydrostatic Axisymmetric Numerical Model. *J. Atmos. Sci.*, **44**, 542-561.

Schubert WH Rozoff CM Vigh JL McNoldy BD Kossin JP. 2007 On the distribution of subsidence in the hurricane eye. *Q. J. R. Meteor. Soc.*, **133**, 595-605.

Shin S Smith RK. 2008 Tropical-cyclone intensification and predictability in a minimal three-dimensional model. *Q. J. R. Meteor. Soc.*, **134**, 1661-1671.

Smith RK. 2006 Accurate determination of a balanced axisymmetric vortex. *Tellus*, **58A**, 98-103.

Smith RK Montgomery MT. 2010 Hurricane boundary-layer theory. *Q. J. R. Meteor. Soc.*, **136**, 1665-1670.

Smith RK Montgomery MT. 2015 Towards clarity on understanding tropical cyclone intensification. *J. Atmos. Sci.*, **72**, 3020-3031.

Smith RK Montgomery MT Nguyen SV. 2009 Tropical cyclone spin up revisited. *Q. J. R. Meteor. Soc.*, **135,** 1321-1335.

Smith RK Schmidt CW Montgomery MT. 2011 An investigation of rotational influences on tropical-cylone size and intensity. *Q. J. R. Meteor. Soc.*, **137**, 1841-1855.

Smith RK Montgomery MT Persing J. 2014a On steady state tropical cyclones. *Q. J. R. Meteor. Soc.*, **140**, 2638-2146.

Smith RK Montgomery MT Thomsen GL. 2014b Sensitivity of tropical cyclone models to the surface drag coefficient in different boundary-layer schemes. *Q. J. R. Meteor. Soc.*, **140**, 792-804.

Weatherford CL Gray WM. 1988 Typhoon structure revealed by aircraft reconnaissance. Part I. Data analysis and climatology. *Mon. Wea. Rev.*, **116**, 1032-1043.

Wirth V Dunkerton TJ. 2006 A unified perspective on the dynamics of hurricanes and monsoons. *J. Atmos. Sci.*, **63**, 2529-2547.

Zhang D-L Black PB French JR Drennan WM 2008 First direct measurements of enthalpy fluxes in the hurricane boundary layer: The CBLAST result. *Geophys. Res. Lett.* **35**, L14813, doi:10.1029/2008GL034374.

Zhu H Smith RK. 2003 Effects of vertical differencing in a minimal hurricane model. *Q. J. R. Meteor. Soc.*, **129**, 1051-1069.

Zhu H Smith RK Ulrich W. 2001 A minimal three-dimensional tropical cyclone model. *J. Atmos. Sci.*, **58**, 1924-1944.